Journal of Materials Chemistry A

ROYAL SOCIETY OF CHEMISTRY

PAPER

View Article Online
View Journal | View Issue

Cite this: *J. Mater. Chem. A*, 2025, **13**, 28129

Composites of isotropic and aligned semiconducting single-walled carbon nanotubes with conjugated polymers for air-processed thermoelectrics

Xabier Rodríguez-Martínez, *[ab] Angus Hawkey,[a] Kevin Bohnet,[a] Sebastian Lindenthal[a] and Jana Zaumseil *[a]

Thermoelectric (TE) materials exploit the Seebeck effect to transform a temperature gradient into a voltage difference and a net current flow. Carbon-based semiconductors such as polymer-sorted single-walled carbon nanotubes (SWCNTs) and conjugated polymers are promising TE candidates that combine unique processing and cost advantages against traditional inorganic counterparts. After the introduction of extrinsic charge carriers *via* doping to improve the TE properties, various strategies exist to further boost the TE performance of organic semiconductors including their alignment and blending in composites. Here, the TE power factor (PF) of isotropic and aligned networks of semiconducting SWCNTs, PBTTT, and their composites are benchmarked for common p-doping with 2,3,5,6-tetrafluoro-7,7,8,8-tetracyanoquinodimethane (F4TCNQ). Composites of SWCNTs and CPs aligned by hot rubbing exhibit superior performance compared to isotropic films. Moreover, the PF increases with the SWCNTs mass ratio in the composites. A PF of 150 ± 20 μW m^{-1} K^{-2} is achieved in these composites upon F4TCNQ doping, which exceeds the figures attained in neat and densely packed SWCNT networks doped with that same molecular acceptor, thus confirming the positive effect of SWCNT/PBTTT blending on TE performance. While F4TCNQ doping is transient, when doping these composites *via* proton-coupled electron transfer in air, the PF remains high (140 ± 30 μW m^{-1} K^{-2}) and stable over at least 60 hours of storage in inert atmosphere. These promising results bring organic TE composites closer to open-air processing as required for applications in printed TE generators.

Received 10th May 2025
Accepted 25th July 2025

DOI: 10.1039/d5ta03744a

rsc.li/materials-a

[a]*Institute for Physical Chemistry, Universität Heidelberg, D-69120 Heidelberg, Germany*

[b]*Universidade da Coruña, Centro de Investigación en Tecnoloxías Navais e Industriais, 15403 Ferrol, Spain. E-mail: xabier.rodriguez@udc.es*

Xabier Rodríguez-Martínez

Dr Xabier Rodríguez-Martínez is UDC-Inditex InTalent Postdoctoral Fellow and Associate Researcher at the University of A Coruña, Spain. After completing his BSc and MSc degrees in nanotechnology (Autonomous University of Barcelona, Spain), he obtained his PhD degree (Materials Science Institute of Barcelona, Spain) for the high-throughput optimization of organic solar cells by combinatorial methods in 2020. Soon after, he moved to Linköping University (Sweden) as a postdoctoral researcher on laminated organic photovoltaics for their integration into buildings. Following this, he earned a Humboldt Postdoctoral Fellowship to develop carbon-based thermoelectric composites at the Institute for Physical Chemistry in Heidelberg University, Germany. His research interests include organic and sustainable electronics for energy harvesting: photovoltaics and thermoelectrics.

1. Introduction

Carbon-based semiconductors are printable and low toxicity thermoelectric (TE) materials capable of converting (waste) heat into electricity. They are particularly suitable for narrow thermal gradients centred at temperatures below 100 °C, and thus for constructing low-temperature energy harvesting modules (*i.e.*, TE generators).[1] Carbon-based semiconductors are often considered to have inherently low thermal conductivity (κ), boosting the TE figure-of-merit defined as $zT = S^2\sigma T\kappa^{-1}$, where S is the Seebeck coefficient, σ the electrical conductivity and T the working temperature. Among carbon-based TE materials, single-walled carbon nanotubes (SWCNTs), conjugated polymers and their composites are promising candidates and have received increasing attention.

SWCNTs can be understood as graphene sheets rolled into seamless tubes, with the rolling-up direction described by a pair of chiral indices (n,m) that eventually determine the electronic (metallic or semiconducting) and optical properties of the nanotube.[2] Due to their quasi-one-dimensional nature, SWCNTs have been proposed as ideal candidates for TE applications.[3] In analogy to conjugated polymers, SWCNTs must be chemically doped to optimize their TE performance.[4] In these materials, p-doping proceeds either *via* charge-transfer with small molecular acceptors (*e.g.*, 2,3,5,6-tetrafluoro-7,7,8,8-tetracyanoquinodimethane, F4TCNQ)[5] or by oxidation using a Lewis acid (*e.g.*, $FeCl_3$,[6] $AuCl_3$),[7] with the possibility to (i) exchange the resulting dopant counterion with electrolyte anions added in excess (*e.g.*, *via* ion-exchange);[8] or (ii) incorporate these electrolyte anions to keep charge neutrality (*e.g.*, in the proton-coupled electron transfer or PCET method).[9] In any case, achieving SWCNT mixtures highly enriched in semiconducting chiralities is of high interest for TE applications. An efficient and scalable method of sorting semiconducting SWCNTs is polymer-wrapping *via* shear force mixing, which yields SWCNT dispersions with >99% semiconducting purity[10] amenable to solution processing into thin films or dense networks by printing[11] or vacuum filtration, respectively. Three-dimensional (3D) networks of polymer-sorted, semiconducting SWCNTs have resulted in record TE power factors (PFs, or $S^2\sigma$) of 920 μW m^{-1} K^{-2}, a figure achieved upon p-doping of small-bandgap nanotubes with dodecaborane clusters.[12] More recently, unsorted SWCNT-based films reached a record PF of 2029 μW m^{-1} K^{-2} through a three-step treatment including the densification of the SWCNT network *via* cold pressing.[13] Notably, these record PFs rival the TE performance achieved in the more widely investigated semiconducting polymers.

Conjugated polymers are rendered attractive for TE applications due to their inherently low κ in isotropic films where molecular disorder dominates the thermal transport.[14] Still, the conjugated backbones contain π-orbitals available for efficient charge transport resulting in competitive σ values for high doping levels.[15] Common polythiophenes derivatives (*e.g.*, P3HT, PBTTT) reach σ close to 50 S cm^{-1} and PFs of *ca.* 100 μW m^{-1} K^{-2} upon p-doping with F4TCNQ,[16] figures that are further improved by using tris(pentafluorophenyl)borane as Brønsted acid dopant (then reaching 230 S cm^{-1} and 140 μW m^{-1} K^{-2} in PBTTT films).[17] By leveraging two-component doping approaches (*e.g.*, ion-exchange[18,19] and Lewis-paired complexes),[20] σ can be significantly enhanced up to 300 S cm^{-1} in isotropic P3HT films.[20] Further TE improvements are usually achieved *via* the orientation of the conjugated backbones, thus resulting in anisotropic TE properties, particularly with respect to the optimization of the PF along the alignment direction.[21] Aligned P3HT films achieve a 3-fold improvement in σ (up to 900 S cm^{-1}) when compared to their isotropic counterparts.[20] Among the existing methods to orient conjugated polymer backbones, hot rubbing has received significant attention and is compatible with the above-mentioned polythiophene derivatives P3HT and PBTTT.[22,23] Notably, hot-rubbed PBTTT-C_{12} films doped with $FeCl_3$ show electrical conductivities as high as 200 000 S cm^{-1} and PFs of 2000 μW m^{-1} K^{-2}.[24] Nevertheless, κ is also expected to increase parallel to the alignment direction, possibly reducing the final zT.[25]

SWCNTs can also be aligned; accordingly, the charge mobility and the TE voltage can be enhanced parallel to the orientation direction.[26,27] The alignment of SWCNTs has been realized by several experimental approaches such as through the functionalization of substrates with amine- and phenyl-terminated silanes,[28] directional blade coating,[29] or gas flow.[30] However, these techniques generally lead to coarse SWCNTs films with poor area coverage and limited percolation pathways for the charge carriers to move efficiently over μm^2 areas (*i.e.*, to make up the channel of a transistor). Thus, a catalogue of techniques derived from the self-assembly,[31–35] shear-induced alignment[36] or controlled vacuum filtration[37] of SWCNTs were developed to yield denser films with well-defined and compact uniaxial orientation. This was recently demonstrated to occur over wafer-scale areas.[38–40]

Composite strategies where SWCNTs are blended with a conjugated polymer matrix are a possible route to further enhance the PF of organic TE materials.[2] On the one hand, the formation of an energy barrier between the SWCNTs and the conjugated polymers could potentially lead to higher S than the individual materials.[13,41] On the other hand, the κ of the composite can be arguably downgraded with respect to neat SWCNT networks (1–5 W m^{-1} K^{-1})[42] and conjugated polymer films (0.2–1.0 W m^{-1} K^{-1})[14] due to enhanced phonon scattering.[43] The co-deposition of SWCNTs and P3HT in the form of hybrid films has yielded PFs of 267 ± 38 μW m^{-1} K^{-2},[44] while sequential overcoating steps of CNTs and conjugated polymers have led to an impressive TE performance of 1825 μW m^{-1} K^{-2}.[45]

A synergy of the abovementioned TE optimization strategies suggests the realization of anisotropic composites where at least one of the active components is purposedly aligned to maximize the TE performance. Few reports exist, though, on exploiting SWCNT/polymer composites for TEs that jointly exploit the expected improvements due to blending and aligning simultaneously. Shear-aligned CNTs have been employed as fillers in combination with PEDOT:PSS[46] or P3HT[47] films prepared by spin-(over)coating. These, in combination with suitable dopants, reached PFs up to 110 μW m^{-1} K^{-2} which are at least

twice as high in untreated, isotropic samples.[47] More recently, SWCNTs embedded in a poly(vinylidene fluoride-trifluoroethylene) polymer matrix have been introduced and showed to incorporate aligned SWCNTs by an AC electric field.[48] Following this rationale, a combination of hot-rubbed SWCNTs with polymer layer overcoatings represents a yet underexplored avenue in the search of competitive TE SWCNT/polymer composites that preserve the processing and low toxicity advantages inherent to organic semiconductors.

In this work, the TE performance of isotropic and aligned semiconducting SWCNTs, conjugated polymers (PBTTT) and their corresponding composites are benchmarked. It is first observed that the dip-coating-driven self-assembly of polymer-wrapped SWCNTs leads to underperforming TE metrics as compared to spin-coated or vacuum-filtered controls. On the contrary, PBTTT films are observed to benefit from the alignment process induced by hot temperature rubbing. SWCNT/PBTTT TE composites are then explored in two different forms: either as a SWCNT/PBTTT bilayer, or as a dense SWCNT network infiltrated with polymer. The bilayer is found to be amenable to orientation *via* hot rubbing, in which case both the SWCNTs and the PBTTT chains are observed to orient in the same direction. In these rubbed, thin composites, the PF upon F4TCNQ doping reaches 48 ± 3 μW m^{-1} K^{-2}, a figure that is further enhanced as soon as the underlying spin-coated SWCNT layer is substituted by a denser, vacuum-filtered network. In this latter case, hot rubbing is observed to no longer yield anisotropic TE properties due to the locked-in morphology of the SWCNT network beneath. Reassuringly, the record PF achieved (150 ± 20 μW m^{-1} K^{-2}) is observed to overcome the value achieved in neat SWCNT networks (140 ± 10 μW m^{-1} K^{-2}), thus confirming the positive TE effect of blending SWCNTs and conjugated polymers. Finally, the PCET doping method, which occurs entirely in air and using aqueous doping solutions, leads to a record PF of 140 ± 30 μW m^{-1} K^{-2}. Importantly, the PF remains virtually unaltered over a period of 60 hours of storage in inert atmosphere regardless of the SWCNT-to-polymer ratio, indicating the promising stability of this new type of organic composite, which is processed and doped entirely in ambient air.

2. Results and discussion

2.1 Processing and TE properties of semiconducting SWCNTs in isotropic and aligned forms

The TE properties of semiconducting SWCNTs were evaluated for three different form factors: spin-coated, aligned (by dip-coating) and vacuum-filtered to form 3D networks. The semiconducting SWCNTs used in this work were obtained by shear-force mixing of plasma torch (PT) SWCNTs in toluene and in the presence of poly[(9,9-dioctylfluorenyl-2,7-diyl)-*alt*-(6,6′-(2,2′-bipyridine))] (PFO-BPy), which selectively wraps semiconducting SWCNTs as reported elsewhere.[10] After filtration to remove excess PFO-BPy and redispersion (in toluene) of the polymer-wrapped SWCNTs, the UV-vis absorbance spectrum shown in Fig. 1a (orange curve) reveals the coexistence of many semiconducting SWCNT chiralities as indicated by several E_{11}, E_{22} and E_{33} absorbance peaks located at *ca.* 1600–1640 nm, 900–1000 nm and 420–520 nm, respectively. The absorption of residual PFO-BPy is also visible at *ca.* 350–360 nm. The high semiconducting purity and absence of metallic nanotubes were confirmed by the lack of absorption peaks in the region of 600–730 nm,[49] and by the corresponding resonant Raman spectra shown in Fig. S1, SI.[50,51] Overall, semiconducting SWCNTs with a typical diameter of 1.17–1.55 nm and a bandgap of 0.70–0.88 eV were obtained by the shear-force mixing process in the presence of PFO-BPy.[52,53]

For the preparation of spin-coated SWCNTs, multiple successive steps of coating were performed on a bare glass substrate to achieve a dense layer with a typical thickness of 1.8 ± 0.6 nm. As observed in the atomic force microscopy (AFM) images of Fig. S2, SI, spin-coating is inefficient for creating very thick and 3D SWCNT networks but effective for laterally-dense layers and removing excess polymer from the film. The efficient formation of thicker (20–80 nm) and vertically dense SWCNT films was achieved by filtration of the SWCNT dispersion (in toluene) onto a mixed cellulose ester (MCE) membrane as described previously.[8,9] By cutting the MCE membrane into the desired shape, SWCNT film patterning and transferring onto a substrate are possible. After dissolving the membrane in an acetone bath, a dense 3D network of SWCNTs is obtained (Fig. S3a, SI).

Finally, thin layers of aligned SWCNTs were obtained by a modified approach inspired by the previous work from Liu *et al.*[40] Herein, two glass substrates were placed vertically in a cuvette filled with *ca.* 7 mL of PT SWCNTs dispersed in 1,1,2-trichloroethane (TCE, with their UV-vis absorbance spectrum shown in Fig. 1a, brown curve) while leaving a gap of 3 mm in between them. Following, a 10–20 μL droplet of *trans*-2-butene-1,4-diol was gently added in the gap, followed by withdrawing both substrates at a speed of 1 μm s^{-1} (Fig. 1b). After repeatedly rinsing in hot toluene, the resulting film morphology (evaluated by AFM, Fig. 1b) and polarized Raman measurements (polar plot of the G^+ band in Fig. 1b and Raman spectra shown in Fig. S4, SI) supported the self-assembly of densely packed and well-aligned SWCNTs. Interestingly, TCE was observed to photobleach the E_{11} absorption peak of the PT SWCNTs while smoothening the remaining absorption features of the E_{22} and E_{33} peaks (brown curve in Fig. 1a), which suggests spontaneous SWCNTs doping[7,54] after redispersion in TCE[55,56] further confirmed by TE measurements (Fig. S2c, SI).

The film absorbance of SWCNTs in different form factors are depicted in Fig. 1c. All films showed broadening of the absorption peaks and smoothed overall features (E_{22} and E_{33} peaks) compared with the dispersions (Fig. 1a), which might result from spontaneous p-doping of the PT SWCNTs as they are processed in air. Filtered 3D network films were the thickest, spin-coated films were the thinnest, while the aligned SWCNT films showed optical anisotropy, which was further confirmed with anisotropic TE measurements (*vide infra*).

All SWCNT films were p-doped using 2,3,5,6-tetrafluoro-7,7,8,8-tetracyanoquinodimethane (F4TCNQ). The TE properties of F4TCNQ-doped spin-coated SWCNT films were first evaluated as a function of time. Doping was performed by

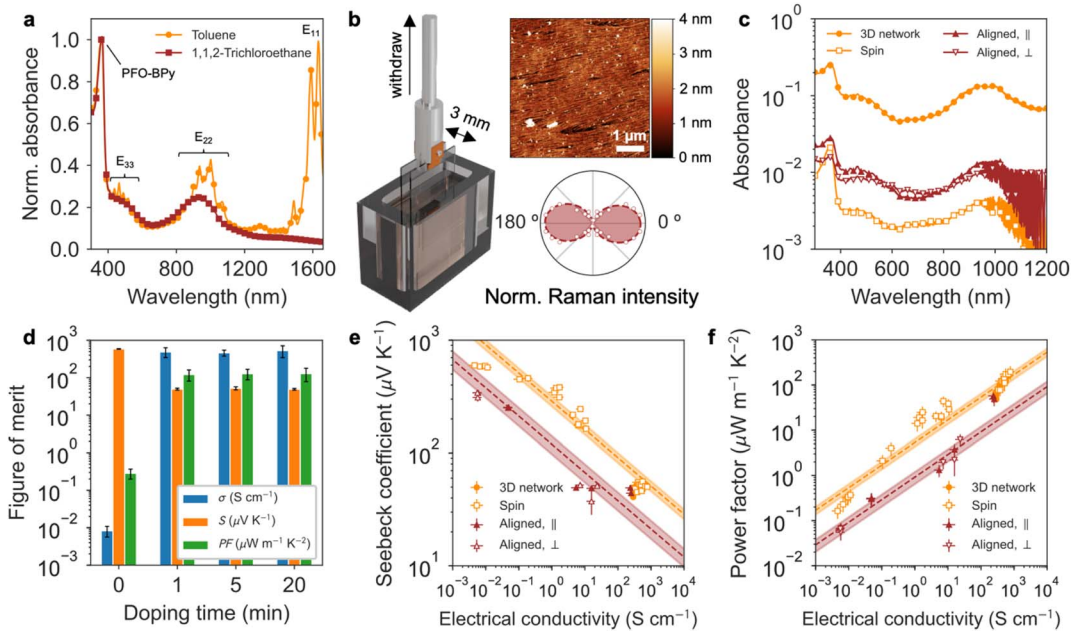

Fig. 1 (a) Normalized absorbance spectra of polymer-wrapped PT SWCNTs dispersed in toluene and TCE. (b) Dip coating setup used to align SWCNTs on two bare glass substrates placed 3 mm apart. AFM image of the aligned SWCNTs and (polarized) Raman intensity polar plot (normalized) of their G^+ band. (c) Absorbance of SWCNT films on glass obtained *via* spin-coating, dip coating (polarized), and vacuum-filtration on an MCE membrane (3D network). (d) TE properties (σ, S, and PF) of spin-coated SWCNT films as a function of doping time with F4TCNQ dissolved in ACN at 1 mg mL^{-1}. (e) S and (f) PF as a function of σ of SWCNT films in different form factors. Dashed lines and shaded areas represent fits and $\pm 2\sigma$ confidence intervals of the empirical $\frac{1}{4}$ power law to the experimental data, respectively.

immersing SWCNT films in 1 mg mL^{-1} solution of the dopant in acetonitrile (ACN) for varying durations (Fig. 1d). Fig. 1d shows that the improvement of the TE properties plateaus very rapidly as there is no statistical difference in the σ, S and PF values obtained after doping for 1 or 20 minutes: 500 ± 100 or 500 ± 200 S cm^{-1}, 50 ± 3 or 50 ± 2 μV K^{-1} and 120 ± 40 or 130 ± 50 μW m^{-1} K^{-2}, respectively. In either case, the formation of F4TCNQ aggregates was observed in the corresponding AFM images (Fig. S5, SI). Fig. 1e and f depict the S and the PF, respectively, as a function of σ of the different SWCNT sample form factors after F4TCNQ doping. The dataset was split into two categories, namely, isotropic (orange data points) and anisotropic (brown data points) films. Note that an implicit classification is also taking place as the isotropic (aligned) samples were processed from toluene (TCE). These were fitted independently to an empirical $\frac{1}{4}$ power law[57] for the S (and $\frac{1}{2}$ power law for the PF; dashed line and shaded areas in Fig. 1e and f, respectively), where

$$S = \frac{k_B}{q}\left(\frac{\sigma}{\sigma_0}\right)^{-1/4} \quad (1)$$

and k_B is the Boltzmann constant, q the elementary charge, and σ_0 the fitting parameter. Fig. 1e and f reveal that the TE properties of the dip-coating-aligned SWCNTs are not superior to those of spin-coated or dense 3D networks of nanotubes. Quantitatively, the σ_0 of the $\frac{1}{4}$ power law (in SI units) reads 12 000 ± 2000 S m^{-1} and 400 ± 100 S m^{-1} for the isotropic and aligned samples, respectively, which results in a ratio of *ca.* 30 units. On the other hand, the use of a different processing solvent (toluene *vs.* TCE) was not observed to limit the maximum achievable TE performance upon F4TCNQ doping (Fig. S6, SI). It is hypothesized that a poor sample homogeneity over the active area used to measure the TE properties (1 mm gap between Au electrodes of 7 mm width, or 7 mm^2) severely downgraded the performance of aligned SWCNTs compared with isotropic SWCNT films. Comparatively, field-effect transistors featuring channel lengths between 200 and 800 nm and channel widths of 4.3 μm were used in previous reports to evaluate the SWCNT aligned film uniformity,[40] which corresponds to a length scale that is far below the dimensions needed in practical TE applications. Despite their poorer performance, TE anisotropy was evidenced in aligned SWCNT films (Fig. S7, SI). Overall, the record σ and PF values of F4TCNQ-doped SWCNTs were obtained on spin-coated films (800 ± 300 S cm^{-1} and 200 ± 70 μW m^{-1} K^{-2}) and vacuum-filtered networks (530 ± 40 S cm^{-1} and 140 ± 10 μW m^{-1} K^{-2}), the latter being more relevant from a practical point of view due to their potentially higher thickness (>80 nm).

2.2 Processing and TE performance of PBTTT in isotropic and aligned forms

The TE properties of isotropic and aligned PBTTT variants (with either tetradecyl, –C_{14}, or dodecyl, –C_{12}, side chains) doped with F4TCNQ were systematically evaluated before considering composites with SWCNTs. Hot rubbing is a well-known methodology to align PBTTT films and improve their TE performance parallel to the alignment direction.[22] The hot rubbing technique

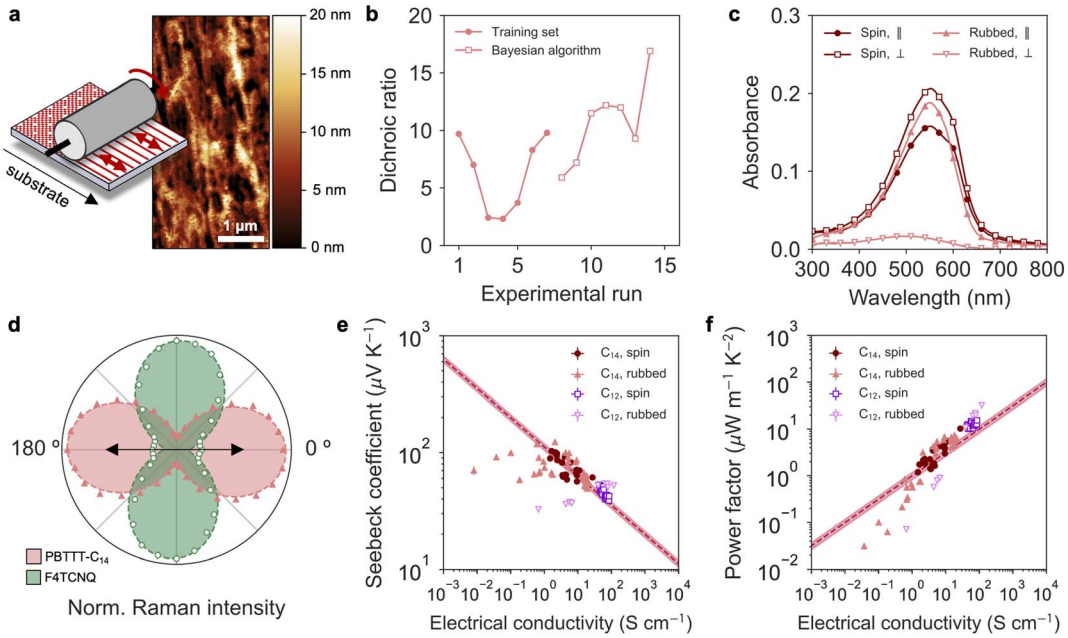

Fig. 2 (a) Sketch of the rubbing setup and AFM image of an aligned PBTTT-C_{14} film after hot rubbing. (b) Evolution of the dichroic ratio of hot-rubbed PBTTT-C_{14} films following a Bayesian optimization algorithm. (c) Polarized absorbance measurements of spin-coated and hot-rubbed PBTTT-C_{14} films. For ∥ (⊥) conditions, the polarization axis was set parallel (perpendicular) to the rubbing direction. (d) Normalized Raman intensity polar plot of characteristic bands of PBTTT-C_{14} and F4TCNQ as observed in a doped rubbed film. The black arrow indicates the rubbing direction. (e) S and (f) PF as a function of σ of PBTTT-C_{14} and PBTTT-C_{12} spin and rubbed films doped with F4TCNQ in ACN at 1 mg mL^{-1}. The dashed line corresponds to a fit of the experimental dataset according to the empirical $\frac{1}{4}$ power law.

was accordingly applied in this work using a homemade setup (Fig. S8, SI), resulting in aligned PBTTT films with the typical rubbed morphology shown in Fig. 2a. The experimental conditions that optimize the dichroic ratio (DR) of the rubbed films were accordingly determined following a Bayesian algorithm (described in the SI), with the training dataset and the results of the Bayesian-inspired experiments shown in Fig. 2b. Said optimization led to the polarized absorbance spectra shown in Fig. 2c for a PBTTT-C_{14} film before and after the rubbing process, as measured parallel (∥) and perpendicular (⊥) to the rubbing direction. These spectra indicate that both a redistribution of the absorption strength and certain material loss occur during the rubbing process resulting in birefringent but inevitably thinner films. Accordingly, the film thickness after the rubbing process was determined by interpolating a calibration curve of the unpolarized absorbance of melt-annealed samples (Fig. S9, SI). Grazing-incidence wide-angle X-ray scattering (GIWAXS) measurements were also performed on spin-coated and rubbed PBTTT-C_{14} films to investigate their texture. The results shown in Fig. S10 and Table S2, SI, confirm that in rubbed PBTTT-C_{14} films the conjugated backbones extend parallel to the rubbing direction while the π-stacking axis arranges in the plane of the sample and perpendicularly to the rubbing direction. Such a spatial interpretation of the crystalline arrangement of PBTTT-C_{14} is in agreement with previous reports on rubbed PBTTT-C_{12}, which suggests that both polymer variants order very similarly in the (rubbed) solid-state.[23]

F4TCNQ-doping of PBTTT films proceeded in an analogue fashion with respect to former SWCNTs, *i.e.*, by dipping in a 1 mg mL^{-1} F4TCNQ solution in ACN. In this case, however, doping time did have a noticeable influence on the TE performance and the absorption spectra, the latter being characterized by the bleaching of the main UV-vis absorption band of the polymer and the formation of a polaron band (Fig. S11a, SI). In this study a doping time of 20 minutes was found to maximize the PF (Fig. S11b, SI) without promoting the formation of dopant aggregates (Fig. S12, SI).

Polarized Raman spectroscopy measurements performed on the F4TCNQ-doped, rubbed PBTTT-C_{14} films indicate an orthogonal dependence of the characteristic Raman modes of the polymer and the dopant (Fig. 2d). This experiment confirms that doping with F4TCNQ preserves the original alignment of the polymer backbone, thus enabling anisotropic TE properties. Fig. 2e and f gather S and PF data, respectively, of spin-coated and rubbed films of PBTTT-C_{14} and PBTTT-C_{12} doped with F4TCNQ and a variety of doping times (1, 5 and 20 minutes). Aligned samples were measured parallel and perpendicular to the rubbing direction although no directional distinction is made in the abovementioned plots (Fig. 2e and f). Instead, the aggregated dataset is fitted according to a $\frac{1}{4}$ power law obtaining a fitting parameter (280 ± 30 S m^{-1}) comparable to that of aligned SWCNTs. Hot rubbing generally leads to improved TE performance compared with spin-coated isotropic, control samples, yet the relative TE improvement and record figures achieved are modest. On the other hand, PBTTT-C_{12} systematically leads to higher σ and PF than the –C_{14} counterpart, an

observation that is in line with previous findings.[21] Accordingly, PBTTT-C_{12} was selected as the benchmark polymer to be blended with SWCNTs in composite bilayers and networks.

2.3 Characterization and TE optimization of F4TCNQ-doped SWCNT/PBTTT composites

Composites of PBTTT-C_{12} and SWCNTs were explored in the form of three variants, namely, (i) a bilayer of spin-coated SWCNTs and PBTTT-C_{12}; (ii) that same bilayer structure after hot rubbing; and (iii) a rubbed 3D network of SWCNTs and PBTTT-C_{12}. The detailed experimental procedures followed to obtain these three types of composites are described in the SI. Polarized Raman spectroscopy was used to investigate the orientation of the SWCNTs, the polymer, and the dopant (F4TCNQ), in the control and composite samples. An exemplary Raman spectrum of a composite sample obtained under 785 nm excitation is shown in Fig. 3a, where the characteristic bands used to track the orientation of the SWCNTs (1583 cm^{-1}), PBTTT-C_{12} (1379 cm^{-1}) and F4TCNQ (1445 cm^{-1}) are also highlighted. In this case, the anisotropy was studied in terms of degree of dichroism (DOD) of the Raman intensity,

$$\mathrm{DOD} = \frac{|I_{\parallel} - I_{\perp}|}{I_{\parallel} + I_{\perp}}, \quad (2)$$

by fitting the Raman spectra collected over the active area (4–7 mm^2, *ca.* 500 fitted spectra per sample) with the polarization set parallel ($I_{\parallel}$) or perpendicular ($I_{\perp}$) to the substrate edge (which is parallel to the rubbing direction, if applicable). Fig. 3b depicts the DOD distribution obtained in benchmark samples in the form of violin plots. Spin-coating is observed to yield isotropic SWCNTs, PBTTT and doped PBTTT films as suggested by the DOD values being tightly distributed around 0.1–0.2. The formation of a bilayer *via* spin-coating in which PBTTT-C_{12} is deposited on top of a previously spin-coated SWCNT layer (followed by F4TCNQ doping) is also observed to preserve an isotropic distribution of the materials (Fig. 3b, spin-coated bilayer case and polar plot in Fig. 3c). Nevertheless, if an analogue (pristine) bilayer is rubbed, both the polymer and the SWCNTs get aligned (DOD = 0.6–0.8) and the subsequently infiltrated F4TCNQ dopant follows a similar DOD distribution (Fig. 3b, rubbed bilayer case and polar plot in Fig. 3d). Based on the corresponding Raman intensity distribution as a function of polarization angle (Fig. 3d), it is argued that (i) both the polymer and the SWCNTs are aligned parallel to the rubbing direction; and (ii) the F4TCNQ lies orthogonally to them (in close analogy to Fig. 2d). Notwithstanding, if the spin-coated SWCNT layer is replaced by a layer of SWCNTs transferred from a vacuum-filtered membrane, where the SWCNTs have a minimum thickness of *ca.* 20 nm (Fig. 3b, rubbed composite network case), an identical rubbing procedure fails to align the sample. Instead, the original isotropic distribution remains (Fig. S13, SI). On the other hand, the broader and significantly higher DOD distribution observed for F4TCNQ in the rubbed composite network suggests that a fraction of the dopant crystallizes, but with limited orientation, plausibly due to a remanent texture that arises due to the mechanical rubbing process.

It is, therefore, concluded that (i) a spin-coated layer of SWCNTs can be oriented by hot rubbing in the presence of a thiophene-based polymer such as PBTTT; and (ii) that as the SWCNTs become thicker and more interpenetrated in a vacuum-filtered 3D network, orientation *via* hot rubbing in the presence of PBTTT is no longer possible and the composite

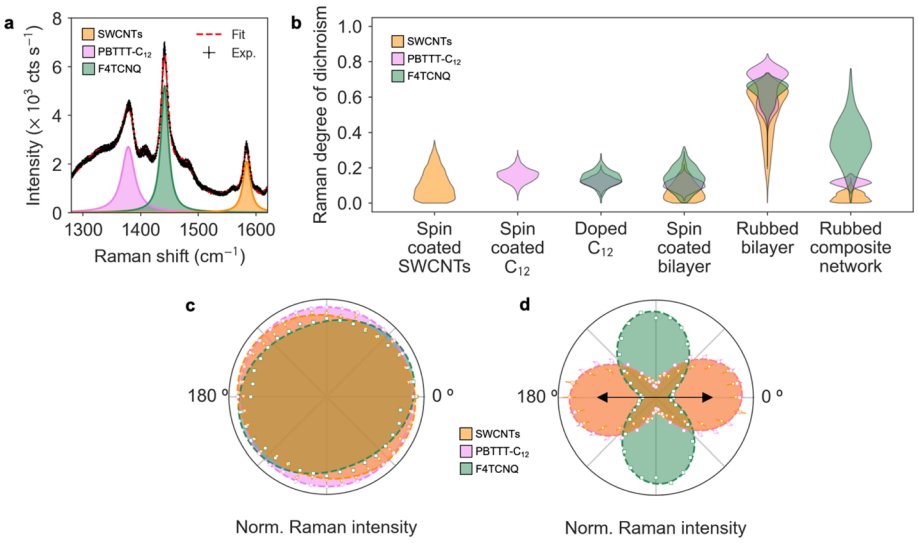

Fig. 3 (a) Exemplary Raman spectrum of an F4TCNQ-doped composite of SWCNTs and PBTTT-C_{12} acquired with 785 nm excitation. The characteristic bands ascribed to SWCNTs (1583 cm^{-1}, orange), PBTTT-C_{12} (1379 cm^{-1}, violet) and F4TCNQ (1445 cm^{-1}, green) appear highlighted. (b) Violin plot illustrating the Raman degree of dichroism of the characteristic material bands following different processing routes. (c) Polar plot of the normalized Raman intensity distribution for each material in a spin-coated and F4TCNQ-doped SWCNT and PBTTT-C_{12} bilayer. (d) Polar plot of the normalized Raman intensity distribution in an F4TCNQ-doped and rubbed bilayer. The black arrow indicates the rubbing direction.

remains in its original isotropic state. These observations suggest that PBTTT can interact strongly with a limited fraction of the SWCNTs and template their orientation by hot rubbing provided a uniform polymer film is formed first atop the SWCNTs, which was confirmed by AFM imaging (Fig. S14, SI). Conversely, in the filtered 3D network of SWCNTs, the polymer is swollen by the network (Fig. S3d, SI), thus preventing an efficient polymer film formation and locking in the isotropic morphology of the pristine and stiff SWCNT network. Even so, the TE performance upon F4TCNQ-doping is superior in the rubbed SWCNT network infiltrated with polymer rather than in the rubbed bilayer despite the observed alignment and TE anisotropy of the latter (*vide infra*).

From an application perspective, charge-transfer with F4TCNQ is an effective yet poorly modulable p-doping method that hardens the identification of the TE sweet spot in terms of PF *vs.* σ. In this case, the adjustment and modulation of the doping level can be coarsely controlled by the concentration of the dopant in the (doping) solution,[58] the doping time[21,59] and/or the thickness of the target film taking into account that F4TCNQ is volatile and might uncontrollably leave and dedope the film.[15] Alternatively, the PF *vs.* σ dependence can be precisely studied by extensive doping first, followed by (temperature-induced) dedoping later. Here, a recently developed platform[9] that allows the parallelization of up to five TE measurements along a single thermal gradient (Fig. 4a) was exploited to draw the corresponding PF curve as a function of σ in rubbed SWCNT/PBTTT-C_{12} networks. In such a setup, an array of five pairs of electrodes was exploited to study the effect that the thickness of the composite network (determined mostly by the thickness of the SWCNT layer, thus controlling the SWCNT : PBTTT ratio) had in the TE properties of the F4TCNQ-doped samples. The setup has a dedicated 20-pin head of gold-coated contacts arranged in quartets in Kelvin geometry, and an Arduino-controlled relay module that electrically switches the connections between adjacent pairs of electrodes. The methodology accelerates the acquisition of data by at least five times compared with traditional one-sample-at-a-time approaches.[9]

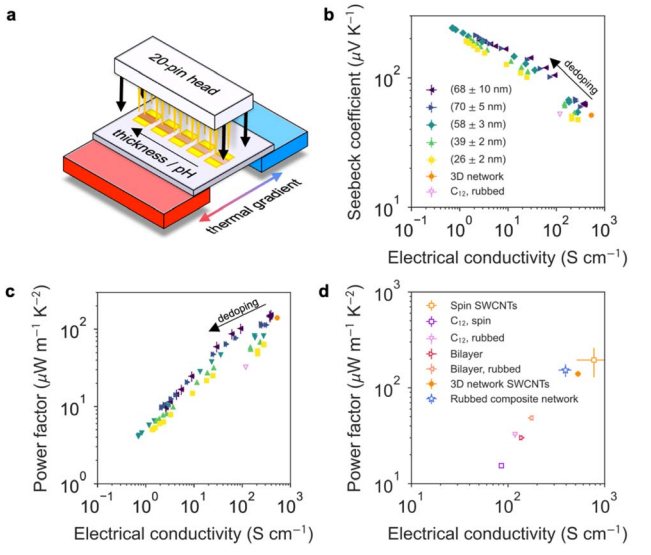

Fig. 4 (a) High-throughput setup used to measure σ and S of up to five samples in parallel across a thermal gradient established in between two Peltier modules. (b) S and (c) PF as a function of σ of F4TCNQ-doped and (thermally) dedoped rubbed networks of SWCNTs and PBTTT-C_{12}. (d) Highest TE PFs obtained among the F4TCNQ-doped samples.

As shown in Fig. 4b and c, composites were F4TCNQ-doped for 20 minutes followed by thermal annealing (140 °C, variable time between 1–4 hours) to induce sample dedoping and trace the dependence between S (Fig. 4b) and PF (Fig. 4c) *vs.* σ. The results showed that (i) the maximum PF is achieved in all cases upon doping for 20 minutes (*i.e.*, freshly doped samples and prior to starting dedoping); (ii) thicker films lead to higher PF and σ; and (iii) that sample thickness leads to different dedoping traces, *i.e.*, thinner films dedope comparatively faster than thicker counterparts. Samples were observed to dedope following two different slopes *vs.* σ as the films became thicker (*cf.*, a single slope modelled the dedoping of the thinnest sample of 26 ± 2 nm), with the inflection point located at *ca.* 60 S cm^{-1}. Due to the sample fabrication procedure, thicker (thinner) films contain a comparatively larger fraction of SWCNTs (PBTTT-C_{12}), a feature that also explains their superior (inferior) PF and maximum achievable σ. Therefore, the observed slope unfolding might reflect an enhanced SWCNT-dominance in the TE properties of the thicker composites. In any case, the optimum performance in terms of PF obtained in neat SWCNT networks and rubbed PBTTT-C_{12} are also shown in Fig. 4b and c. These data indicate that composites (with a record PF of 150 ± 20 μW m^{-1} K^{-2}) significantly increase the TE performance with respect to neat and rubbed PBTTT-C_{12} films (32 ± 2 μW m^{-1} K^{-2}), and that the former value represents a subtle improvement with respect to the optimum PF observed in neat SWCNT 3D networks (140 ± 10 μW m^{-1} K^{-2}).

The TE properties of the here discussed collection of sample form factors were benchmarked after doping with F4TCNQ and following identical experimental conditions (1 mg mL^{-1} of F4TCNQ in ACN for 20 minutes). The resulting champion PFs are shown in Fig. 4d and listed in Table 1. The TE improvement associated to the rubbing process is evident when comparing spin-coated and rubbed samples of PBTTT-C_{12} and SWCNT/PBTTT-C_{12} bilayers: the PF approximately doubles in the pristine polymer scenario (from the original 15.3 ± 0.9 μW m^{-1} K^{-2} up to 32 ± 2 μW m^{-1} K^{-2}) and increases by 60% in the bilayer case (from 30 ± 2 μW m^{-1} K^{-2} to 48 ± 3 μW m^{-1} K^{-2}). However, enhanced performances are obtained in SWCNT-richer samples such as spin-coated SWCNTs (200 ± 70 μW m^{-1} K^{-2}) and vacuum-filtered 3D networks (140 ± 10 μW m^{-1} K^{-2}). Despite their superior PF, the spin-coated SWCNTs have very limited practical application due to their reduced thickness (<2 nm, with significant uncertainty) and inefficient film formation, thus the rubbed composite networks (150 ± 20 μW m^{-1} K^{-2}) are the most promising TE candidates identified in this work. Reassuringly, they show a champion PF that is approximately 10% higher than the best neat 3D network SWCNTs counterpart.

Table 1 Record TE performance (in terms of PF) achieved in a collection of 86 F4TCNQ-doped samples. Note that the listed values of σ and S correspond to those achieved at the sample with maximum PF only

Sample type	Electrical conductivity, σ (S cm^{-1})	Seebeck coefficient, S (μV K^{-1})	Power factor, PF (μW m^{-1} K^{-2})
Spin-coated SWCNTs	800 ± 300	50 ± 1	200 ± 70
Spin-coated PBTTT-C_{12}	85 ± 4	42.4 ± 0.7	15.3 ± 0.9
Rubbed PBTTT-C_{12}	118 ± 7	52 ± 1	32 ± 2
Bilayer w/PBTTT-C_{12}	139 ± 7	47 ± 1	30 ± 2
Rubbed bilayer w/PBTTT-C_{12}	170 ± 10	53 ± 1	48 ± 3
3D network SWCNTs	530 ± 40	51.4 ± 0.6	140 ± 10
Rubbed composite network	390 ± 60	62.5 ± 0.9	150 ± 20

2.4 TE performance of SWCNT/PBTTT composites doped *via* PCET

F4TCNQ is a volatile dopant that is not suitable for longterm doping, hence we have also extended this study to PCET doping using benzoquinone (BQ) as the p-dopant in pH-controlled aqueous solutions.[9,60] BQ is reduced to hydroquinone (HQ) by accepting two electrons from the semiconductor and two protons (H^+) from the buffered solution. Consequently, the semiconductor is oxidized (*i.e.*, p-doped). Due to the charge neutrality of HQ, an additional electrolyte anion is needed to drive the electron transfer, here bis(trifluoromethylsulfonyl) imide (TFSI) added in excess as Li[TFSI]. As the redox potential of the BQ/HQ pair increases with decreasing pH of the buffered solution, PCET allows precise adjustment of the doping level *via* pH. Moreover, since the doping procedure takes place entirely in water and in air it is much more practical than previous methods.

Fig. 5a shows the PF obtained in neat SWCNT networks of varying thickness, and doped by the PCET method, *i.e.*, using BQ as the dopant and $TFSI^-$ as the counterion. Doping occurred reversibly as the pH of the doping solution was varied from 1 to 5 (in unit steps) using the experimental parallelization platform (Fig. 4a). As a benchmark value, the PF obtained in F4TCNQ-doped samples (140 ± 10 μW m^{-1} K^{-2}) is also included in Fig. 5a. Thicker PCET-doped SWCNT networks exhibit higher PF than F4TCNQ-doped networks. PCET doping at pH = 1 leads to a maximum PF of 160 ± 10 μW m^{-1} K^{-2}.

Fig. 5b shows the PF of PBTTT-C_{12} samples and their bilayers with spin-coated SWCNTs doped by PCET. The pH was varied locally at each pair of electrodes using a droplet containing

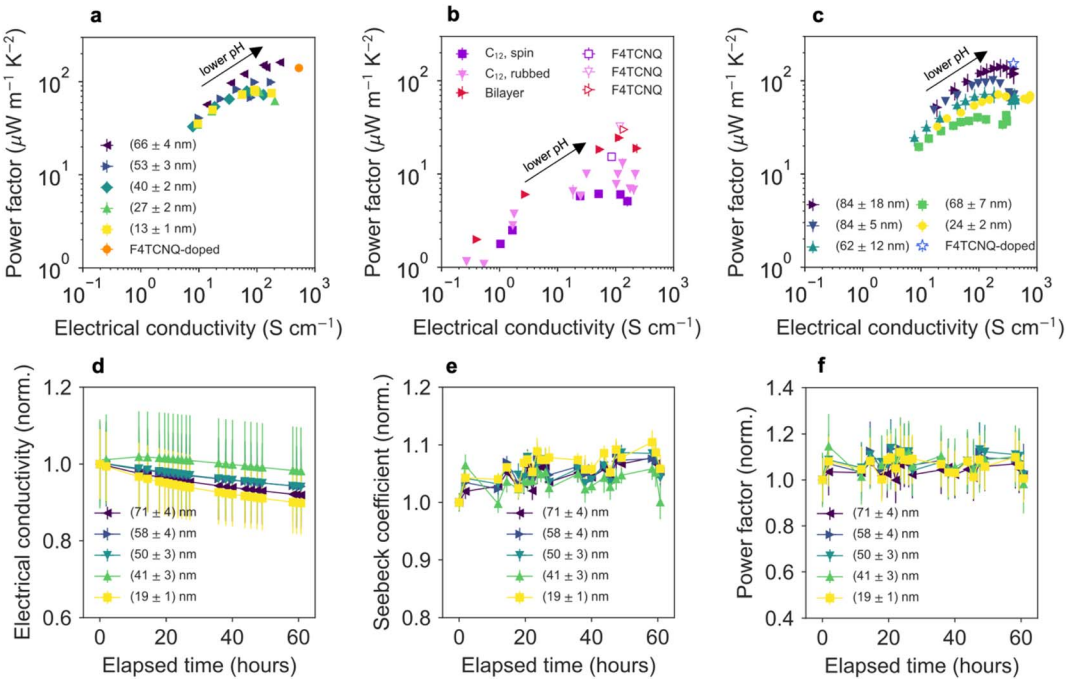

Fig. 5 (a) PF of PCET-doped SWCNT networks of varying thickness. The record PF of F4TCNQ-doped networks is included as a benchmark. (b) PF of PCET-doped PBTTT-C_{12} films and spin-coated SWCNTs/PBTTT-C_{12} bilayers. Open symbols correspond to the champion figures obtained in F4TCNQ-doped samples. (c) PF of PCET-doped composite rubbed networks of SWCNTs and PBTTT-C_{12}. The champion PF obtained in F4TCNQ-doped samples is also included. (d) Normalized σ, (e) S and (f) PF obtained over a period of 60 hours for PCET-doped, rubbed composites of varying thickness.

a buffer solution of adequate pH. Thus, a single substrate was sufficient to create at least 5 PF *versus* σ data points (corresponding to pH 1 to 5 in unit steps). The results confirmed that rubbing of PBTTT-C_{12} increases the PF and σ compared with isotropic and spin-coated films. The creation of a bilayer with SWCNTs underneath the polymer layer further improved the PF. However, the performance achieved remained below that obtained for F4TCNQ-doped samples (Fig. 5b), which indicates the limitations of the use of BQ as the dopant and TFSI as the counterion for PBTTT-C_{12}. The best performance was obtained for PCET doping at pH 2.

PCET-doped SWCNT/PBTTT-C_{12} composite networks were tested as a function of thickness with the best performance for thicker films (84 ± 18 nm in Fig. 5c). For these measurements, σ and PF were tuned by progressively dedoping the films by immersion in deionized water for *ca.* 40 minutes between consecutive data points. The maximum PF (140 ± 30 μW m^{-1} K^{-2}) was reached after a mild dedoping (initial doping state for pH 1), which suggested that a pH of 2–3 should lead to the optimum performance in this type of composite layers. Note that although thicker composites generally lead to higher PF (Fig. 5c), it is still unclear how κ varies as a function of the SWCNT : PBTTT ratio. A smaller fraction of SWCNTs in the composite (which show a comparatively higher κ, 1–5 W m^{-1} K^{-1} in doped dense films,[42] than PBTTT, 1.0 ± 0.1 W m^{-1} K^{-1})[14] will plausibly reduce κ, such that the TE figure of merit zT ($zT = S^2\sigma T\kappa^{-1}$) of the thinner composites might improve. However, further experiments are needed to test this hypothesis.

Due to the promising performance and processing advantages of PCET-doped composites, their longterm stability was evaluated for a period of *ca.* 60 hours while stored without encapsulation in a nitrogen-filled glovebox. The results shown in Fig. 5d–f for a composite doped at pH = 2 indicate promising stability of σ (Fig. 5d), S (Fig. 5e) and PF (Fig. 5f) regardless of sample thickness, with the non-normalized data shown in Fig. S15, SI. σ is observed to slowly decay with time while S increases, thus resulting in a stable PF over the period of the stability assay. Notably, our data suggests that the stability trend might be following the PF *vs.* σ curve traced in Fig. 5c (Fig. S16, SI). This implies that the constant PF might hold for several hundred hours of storage. Hence, precise adjustment of the doping level at or slightly beyond the peak PF (Fig. 5c) is an effective strategy to maximize the lifetime of PCET-doped SWCNT/PBTTT composite films for TE devices.

3. Conclusions

This work benchmarks the TE performance of semiconducting SWCNTs, PBTTT and their composites in a variety of sample form factors, including hot-rubbed composite films in which both SWCNTs and PBTTT backbones become uniaxially oriented to yield anisotropic TE properties. We find that dense thick networks of SWCNTs offer an adequate trade-off between practical sample preparation and TE performance (140 ± 10 μW m^{-1} K^{-2}) compared to thin spin-coated (200 ± 70 μW m^{-1} K^{-2}) or aligned SWCNT films when p-doping with F4TCNQ. PBTTT films generally show improved TE performance after uniaxial alignment *via* hot rubbing. For F4TCNQ-doped PBTTT-C_{12} the PF increases to 32 ± 2 μW m^{-1} K^{-2} along the rubbing direction, compared to 15.3 ± 0.9 μW m^{-1} K^{-2} for spin-coated films.

For a bilayer of PBTTT and SWCNTs, hot rubbing orients both materials with their optical transition dipole parallel to the rubbing direction. Such a composite results in yet another 50% improvement of the TE properties (PF = 48 ± 3 μW m^{-1} K^{-2}) with respect to the neat and oriented PBTTT-C_{12} polymer. Dense SWCNT networks infiltrated with PBTTT-C_{12} and rubbed gave the best TE performance with PF = 150 ± 20 μW m^{-1} K^{-2}, thus slightly outperforming even record values for neat F4TCNQ-doped networks of SWCNTs.

Finally, the PCET doping method (in air and with aqueous solutions) enables PFs of 160 ± 10 μW m^{-1} K^{-2} for neat SWCNT networks and 140 ± 30 μW m^{-1} K^{-2} for the corresponding rubbed composites with PBTTT-C_{12}. PCET-doped films are advantageous from a processing and stability viewpoint with their PF being stable for at least 60 hours in inert atmosphere. This longterm stability of doped SWCNT/polymer films represents an important step toward practical applications of carbon-based TE composites.

Conflicts of interest

There are no conflicts to declare.

Data availability

All data supporting the findings of this study are available within the article and its SI.

Supplementary information (SI) is available including experimental details on the preparation, doping and thermoelectric characterization of thin film samples; Raman spectra of isotropic and aligned single-walled carbon nanotubes; atomic force microscopy images of polymer, single-walled carbon nanotubes, and their (doped) composites; grazing-incidence X-ray diffractograms of aligned polymer films; and non-normalized thermoelectric stability data of relevant composites. See DOI: **https://doi.org/10.1039/d5ta03744a**.

Acknowledgements

X. R.-M. acknowledges funding from the Alexander von Humboldt Foundation (Germany). X. R.-M. acknowledges experimental support from staff at the NCD-SWEET beamline at ALBA Synchrotron (experiment ID AV-2023087673). A. H. and J. Z. acknowledge funding by the European Union's Horizon 2020 research and innovation program under the Marie Skłodowska-Curie grant agreement no. 955837 (HORATES). The authors thank Klaus Schmitt and Günter Meinusch for their support in building the rubbing machine.

References

1 M. Massetti, F. Jiao, A. J. Ferguson, D. Zhao, K. Wijeratne, A. Würger, J. L. Blackburn, X. Crispin and S. Fabiano, *Chem. Rev.*, 2021, **121**, 12465–12547.

2 J. L. Blackburn, A. J. Ferguson, C. Cho and J. C. Grunlan, *Adv. Mater.*, 2018, **30**, 1704386.
3 L. D. Hicks and M. S. Dresselhaus, *Phys. Rev. B: Condens. Matter Mater. Phys.*, 1993, **47**, 16631–16634.
4 Y. Liu, Z. Zhao, L. Kang, S. Qiu and Q. Li, *Small*, 2024, **20**, 2304075.
5 N. J. Stanton, R. Ihly, B. Norton-Baker, A. J. Ferguson and J. L. Blackburn, *Appl. Phys. Lett.*, 2021, **119**, 023302.
6 Y. Liu, W. Yang, A. Sharma, D. Rosas-Villalva, H. Xu, M. A. Haque, F. Laquai and D. Baran, *Adv. Electron. Mater.*, 2024, 2400216.
7 K. H. Eckstein, F. Oberndorfer, M. M. Achsnich, F. Schöppler and T. Hertel, *J. Phys. Chem. C*, 2019, **123**, 30001–30006.
8 A. Hawkey, A. Dash, X. Rodríguez-Martínez, Z. Zhao, A. Champ, S. Lindenthal, M. Zharnikov, M. Kemerink and J. Zaumseil, *Adv. Mater.*, 2024, 2404554.
9 A. Hawkey, X. Rodríguez-Martínez, S. Lindenthal, M. C. F. Jansen, R. Crispin and J. Zaumseil, *Adv. Electron. Mater.*, 2025, 2400817.
10 A. Graf, Y. Zakharko, S. P. Schießl, C. Backes, M. Pfohl, B. S. Flavel and J. Zaumseil, *Carbon*, 2016, **105**, 593–599.
11 M. Rother, M. Brohmann, S. Yang, S. B. Grimm, S. P. Schießl, A. Graf and J. Zaumseil, *Adv. Electron. Mater.*, 2017, **3**, 1700080.
12 T. L. Murrey, T. J. Aubry, O. L. Ruiz, K. A. Thurman, K. H. Eckstein, E. A. Doud, J. M. Stauber, A. M. Spokoyny, B. J. Schwartz, T. Hertel, J. L. Blackburn and A. J. Ferguson, *Cell Rep. Phys. Sci.*, 2023, **4**, 101407.
13 Y.-M. Liu, X.-L. Shi, T. Wu, H. Wu, Y. Mao, T. Cao, D.-Z. Wang, W.-D. Liu, M. Li, Q. Liu and Z.-G. Chen, *Nat. Commun.*, 2024, **15**, 3426.
14 X. Rodríguez-Martínez, F. Saiz, B. Dörling, S. Marina, J. Guo, K. Xu, H. Chen, J. Martin, I. McCulloch, R. Rurali, J. S. Reparaz and M. Campoy-Quiles, *Adv. Energy Mater.*, 2024, **14**, 2401705.
15 A. D. Scaccabarozzi, A. Basu, F. Aniés, J. Liu, O. Zapata-Arteaga, R. Warren, Y. Firdaus, M. I. Nugraha, Y. Lin, M. Campoy-Quiles, N. Koch, C. Müller, L. Tsetseris, M. Heeney and T. D. Anthopoulos, *Chem. Rev.*, 2022, **122**, 4420–4492.
16 O. Zapata-Arteaga, S. Marina, G. Zuo, K. Xu, B. Dörling, L. A. Pérez, J. S. Reparaz, J. Martín, M. Kemerink and M. Campoy-Quiles, *Adv. Energy Mater.*, 2022, **12**, 2104076.
17 J. Kim, D. Ju, S. Kim and K. Cho, *Adv. Funct. Mater.*, 2024, **34**, 2309156.
18 I. E. Jacobs, Y. Lin, Y. Huang, X. Ren, D. Simatos, C. Chen, D. Tjhe, M. Statz, L. Lai, P. A. Finn, W. G. Neal, G. D'Avino, V. Lemaur, S. Fratini, D. Beljonne, J. Strzalka, C. B. Nielsen, S. Barlow, S. R. Marder, I. McCulloch and H. Sirringhaus, *Adv. Mater.*, 2022, **34**, 2102988.
19 Y. Yamashita, J. Tsurumi, M. Ohno, R. Fujimoto, S. Kumagai, T. Kurosawa, T. Okamoto, J. Takeya and S. Watanabe, *Nature*, 2019, **572**, 634–638.
20 O. Zapata-Arteaga, A. Perevedentsev, M. Prete, S. Busato, P. S. Floris, J. Asatryan, R. Rurali, J. Martín and M. Campoy-Quiles, *ACS Energy Lett.*, 2024, **9**, 3567–3577.
21 V. Vijayakumar, E. Zaborova, L. Biniek, H. Zeng, L. Herrmann, A. Carvalho, O. Boyron, N. Leclerc and M. Brinkmann, *ACS Appl. Mater. Interfaces*, 2019, **11**, 4942–4953.
22 L. Biniek, N. Leclerc, T. Heiser, R. Bechara and M. Brinkmann, *Macromolecules*, 2013, **46**, 4014–4023.
23 Y. Huang, D. H. Lukito Tjhe, I. E. Jacobs, X. Jiao, Q. He, M. Statz, X. Ren, X. Huang, I. McCulloch, M. Heeney, C. McNeill and H. Sirringhaus, *Appl. Phys. Lett.*, 2021, **119**, 111903.
24 V. Vijayakumar, Y. Zhong, V. Untilova, M. Bahri, L. Herrmann, L. Biniek, N. Leclerc and M. Brinkmann, *Adv. Energy Mater.*, 2019, **9**, 1900266.
25 T. Degousée, V. Untilova, V. Vijayakumar, X. Xu, Y. Sun, M. Palma, M. Brinkmann, L. Biniek and O. Fenwick, *J. Mater. Chem. A*, 2021, **9**, 16065–16075.
26 K. Fukuhara, Y. Ichinose, H. Nishidome, Y. Yomogida, F. Katsutani, N. Komatsu, W. Gao, J. Kono and K. Yanagi, *Appl. Phys. Lett.*, 2018, **113**, 243105.
27 S. M. Mirza and H. Grebel, *Appl. Phys. Lett.*, 2008, **92**, 203116.
28 M. C. LeMieux, M. Roberts, S. Barman, Y. W. Jin, J. M. Kim and Z. Bao, *Science*, 2008, **321**, 101–104.
29 V. Derenskyi, W. Gomulya, J. M. S. Rios, M. Fritsch, N. Fröhlich, S. Jung, S. Allard, S. Z. Bisri, P. Gordiichuk, A. Herrmann, U. Scherf and M. A. Loi, *Adv. Mater.*, 2014, **26**, 5969–5975.
30 H. Xin and A. T. Woolley, *Nano Lett.*, 2004, **4**, 1481–1484.
31 K. R. Jinkins, S. M. Foradori, V. Saraswat, R. M. Jacobberger, J. H. Dwyer, P. Gopalan, A. Berson and M. S. Arnold, *Sci. Adv.*, 2021, **7**, eabh0640.
32 Y. Joo, G. J. Brady, M. S. Arnold and P. Gopalan, *Langmuir*, 2014, **30**, 3460–3466.
33 T. A. Shastry, J. T. Seo, J. J. Lopez, H. N. Arnold, J. Z. Kelter, V. K. Sangwan, L. J. Lauhon, T. J. Marks and M. C. Hersam, *Small*, 2013, **9**, 45–51.
34 K. R. Jinkins, J. H. Dwyer, A. Suresh, S. M. Foradori, P. Gopalan and M. S. Arnold, *Langmuir*, 2023, **39**, 14433–14440.
35 K. R. Jinkins, J. Chan, G. J. Brady, K. K. Gronski, P. Gopalan, H. T. Evensen, A. Berson and M. S. Arnold, *Langmuir*, 2017, **33**, 13407–13414.
36 K. R. Jinkins, J. Chan, R. M. Jacobberger, A. Berson and M. S. Arnold, *Adv. Electron. Mater.*, 2019, **5**, 1800593.
37 N. Komatsu, M. Nakamura, S. Ghosh, D. Kim, H. Chen, A. Katagiri, Y. Yomogida, W. Gao, K. Yanagi and J. Kono, *Nano Lett.*, 2020, **20**, 2332–2338.
38 X. He, W. Gao, L. Xie, B. Li, Q. Zhang, S. Lei, J. M. Robinson, E. H. Hároz, S. K. Doorn, W. Wang, R. Vajtai, P. M. Ajayan, W. W. Adams, R. H. Hauge and J. Kono, *Nat. Nanotechnol.*, 2016, **11**, 633–638.
39 C. Rutherglen, A. A. Kane, P. F. Marsh, T. A. Cain, B. I. Hassan, M. R. AlShareef, C. Zhou and K. Galatsis, *Nat. Electron.*, 2019, **2**, 530–539.
40 L. Liu, J. Han, L. Xu, J. Zhou, C. Zhao, S. Ding, H. Shi, M. Xiao, L. Ding, Z. Ma, C. Jin, Z. Zhang and L.-M. Peng, *Science*, 2020, **368**, 850–856.

41 Y. Zhang, Q. Zhang and G. Chen, *Carbon Energy*, 2020, **2**, 408–436.
42 D. J. Wesenberg, M. J. Roos, A. D. Avery, J. L. Blackburn, A. J. Ferguson and B. L. Zink, *Adv. Electron. Mater.*, 2020, **6**, 2000746.
43 E. Muchuweni and E. T. Mombeshora, *Appl. Surf. Sci. Adv.*, 2023, **13**, 100379.
44 C. T. Hong, W. Lee, Y. H. Kang, Y. Yoo, J. Ryu, S. Y. Cho and K.-S. Jang, *J. Mater. Chem. A*, 2015, **3**, 12314–12319.
45 C. Cho, B. Stevens, J. Hsu, R. Bureau, D. A. Hagen, O. Regev, C. Yu and J. C. Grunlan, *Adv. Mater.*, 2015, **27**, 2996–3001.
46 K. Yusupov, S. Stumpf, S. You, A. Bogach, P. M. Martinez, A. Zakhidov, U. S. Schubert, V. Khovaylo and A. Vomiero, *Adv. Funct. Mater.*, 2018, **28**, 1801246.
47 S. Mardi, K. Yusupov, P. M. Martinez, A. Zakhidov, A. Vomiero and A. Reale, *ACS Omega*, 2021, **6**, 1073–1082.
48 H. Joh, G. Anoop, S. Jo, W. Seol, S. M. Park, K. Eom, H. J. Lee and J. Y. Jo, *ACS Appl. Energy Mater.*, 2025, **8**, 3178–3184.
49 J. Ding, Z. Li, J. Lefebvre, F. Cheng, G. Dubey, S. Zou, P. Finnie, A. Hrdina, L. Scoles, G. P. Lopinski, C. T. Kingston, B. Simard and P. R. L. Malenfant, *Nanoscale*, 2014, **6**, 2328.
50 R. B. Weisman and S. M. Bachilo, *Nano Lett.*, 2003, **3**, 1235–1238.
51 H. Kataura, Y. Kumazawa, Y. Maniwa, I. Umezu, S. Suzuki, Y. Ohtsuka and Y. Achiba, *Synth. Met.*, 1999, **103**, 2555–2558.
52 K. S. Mistry, B. A. Larsen and J. L. Blackburn, *ACS Nano*, 2013, **7**, 2231–2239.
53 M. Brohmann, M. Rother, S. P. Schießl, E. Preis, S. Allard, U. Scherf and J. Zaumseil, *J. Phys. Chem. C*, 2018, **122**, 19886–19896.
54 M. A. Hermosilla-Palacios, M. Martinez, E. A. Doud, T. Hertel, A. M. Spokoyny, S. Cambré, W. Wenseleers, Y.-H. Kim, A. J. Ferguson and J. L. Blackburn, *Nanoscale Horiz.*, 2024, **9**, 278–284.
55 K. R. Moonoosawmy and P. Kruse, *J. Am. Chem. Soc.*, 2008, **130**, 13417–13424.
56 P. Taborowska, G. Stando, M. Sahlman, M. Krzywiecki, M. Lundström and D. Janas, *Sci. Rep.*, 2022, **12**, 7004.
57 A. M. Glaudell, J. E. Cochran, S. N. Patel and M. L. Chabinyc, *Adv. Energy Mater.*, 2015, **5**, 1401072.
58 A. Hamidi-Sakr, L. Biniek, J. Bantignies, D. Maurin, L. Herrmann, N. Leclerc, P. Lévêque, V. Vijayakumar, N. Zimmermann and M. Brinkmann, *Adv. Funct. Mater.*, 2017, **27**, 1700173.
59 S. N. Patel, A. M. Glaudell, K. A. Peterson, E. M. Thomas, K. A. O'Hara, E. Lim and M. L. Chabinyc, *Sci. Adv.*, 2017, **3**, e1700434.
60 M. Ishii, Y. Yamashita, S. Watanabe, K. Ariga and J. Takeya, *Nature*, 2023, **622**, 285–291.